INTERNATIONAL JOURNAL FOR NUMERICAL METHODS IN ENGINEERING
*Int. J. Numer. Meth. Engng* 2005; **62**:899–923
Published online 2 December 2004 in Wiley InterScience (www.interscience.wiley.com). DOI: 10.1002/nme.1196

# Anisotropic adaptive simulation of transient flows using discontinuous Galerkin methods

Jean-François Remacle[1,*,†], Xiangrong Li[2],
Mark S. Shephard[2] and Joseph E. Flaherty[2]

[1]*Département de Génie Civil et Environnemental, Université Catholique de Louvain, Bâtiment Vinci, Place du Levant 1, B-1348 Louvain-la-Neuve, Belgium*
[2]*Scientific Computation Research Center, Rensselaer Polytechnic Institute, Troy, NY, 12180-3590, U.S.A.*

SUMMARY

An anisotropic adaptive analysis procedure based on a discontinuous Galerkin finite element discretization and local mesh modification of simplex elements is presented. The procedure is applied to transient two- and three-dimensional problems governed by Euler's equation. A smoothness indicator is used to isolate jump features where an aligned mesh metric field in specified. The mesh metric field in smooth portions of the domain is controlled by a Hessian matrix constructed using a variational procedure to calculate the second derivatives. The transient examples included demonstrate the ability of the mesh modification procedures to effectively track evolving interacting features of general shape as they move through a domain. Copyright © 2004 John Wiley & Sons, Ltd.

KEY WORDS: anisotropic adaptive; discontinuous Galerkin; mesh modification

## 1. INTRODUCTION

The appropriate means to ensure that a mesh-based numerical analysis procedure produces the most effective solution results is to apply an adaptive solution strategy. Efforts on the development of these techniques have been underway for over 20 years and have provided a number of important theoretical and practical results. However, these methods have not yet found their way into common practice for a number of reasons. Among the reasons for the slow acceptance is the lack of clear evidence that their implementations to be able to deal with entirely general domains and solution fields in a computationally effective manner.

*Correspondence to: J.-F. Remacle, Département de Génie Civil et Environnemental, Université Catholique de Louvain, Bâtiment Vinci, Place du Levant 1, B-1348 Louvain-la-Neuve, Belgium.
†E-mail: remacle@gce.ucl.ac.be

*Received 9 September 2003*
*Revised 15 January 2004*
*Accepted 26 July 2004*

In cases where the solution field is characterized by strong directional gradients, the effective solution requires the adaptive creation of anisotropic mesh configurations. The paper presents a set of procedures to create adaptively defined anisotropic meshes over general two- and three-dimensional domains and demonstrates its application in transient flow simulations.

The three ingredients of an anisotropic adaptive procedure are:

- the equation discretization technology,
- the anisotropic mesh correction indication procedures that use the analysis results to determine, where and how to modify the mesh to reach the desired level of accuracy, and
- the anisotropic mesh adaptation procedure to create a mesh configuration consistent with the mesh distribution the correction indication procedures have defined.

A number of finite element and finite volume discretization technologies are amenable to use with anisotropic meshes. In the present paper the applications considered are flow problems modelled using conservation laws and characterized by having moving features such as shocks. Therefore, the discontinuous Galerkin (DG) [1] finite element formulation given in Section 2 was selected for equation discretization. In addition to being well suited to the resolution of solution fields with discontinuities, the DG formulations provide flexibility in the selection of basis function leading to more effective numerical solution and can be effectively parallelized due to the order independent nearest neighbour only interactions [2]. One complication of the application of DG methods is their discontinuous nature does complicate the effective calculation of the second order derivative quantities used by most anisotropic adaptive procedure. The approach used in the current paper to address the evaluation of these derivatives is discussed in Section 3.2.

Recently a number of investigators have begun to consider the various components of the construction of anisotropic adaptive analysis procedures [3–14]. Ideally an adaptive analysis procedure would employ a bounded estimate [15, 16] of the discretization error. Since such estimates are based on elemental level contributions, they have typically been used to determine where and how to improve the mesh when isotropic mesh refinement is used. For many classes of equations of interest bounded error estimates are not yet available. However, this does not preclude the use of simple error indicators based on various gradient measurements from providing useful adaptive procedures [17–20]. A second complexity that arises in anisotropic adaptive procedures is that even when available, the bounded error estimates are typically scalar norms that do not provide the directional information needed to define the desired mesh anisotropy. Therefore, anisotropic adaptive procedures employ the full set of second order derivatives (Hessian matrix) [4, 6, 12] or examine derivatives in the direction of specific mesh entities (typically edges) [9, 14] to obtain directional information on the desired mesh layout. For purposes of this discussion the term mesh correction indicator is used to describe this information after it had been scaled to define the actual anisotropic element sizes desired over the domain. Section 3 discusses the procedures that constitute the mesh correction indicator used in this paper to define the anisotropic adaptive mesh size field.

Given the new mesh size field, there are the two means to construct a mesh that satisfies it. They are to regenerate the mesh against that mesh size field [3, 4, 6, 12], or to perform appropriate local mesh modifications to match the desired mesh size field [9–11, 14]. The remeshing based techniques have the advantage of not being constrained by the existence of the previous mesh entities in the construction of the new anisotropic mesh configuration. However, these methods do incur the cost of a complete mesh generation step and, in many

 

applications, require the application of a solution field transfer process between meshes which is both expensive and subject to accuracy loss. Mesh modification procedures can be executed quickly with more controlled solution transfer procedures. However, with only a limited set of mesh modification operations allowed, the mesh configurations are not optimal. Of course, with the inclusion of a 'full set' of mesh modification operations (e.g. like the procedure in Reference [10]) the differences in the final mesh configuration between remeshing and mesh modification can essentially be eliminated. The procedure used in this work (see Section 4) applies a 'full set' of mesh modification operators employing a set of intelligent heuristics to effectively determine the appropriate mesh modifications to obtain the desired mesh configurations. Section 5 presents a set of two- and three-dimensional transient flow simulations to demonstrate the power of the method to solve flow problems with complex evolving features.

## 2. DISCONTINUOUS GALERKIN FORMULATION

Consider an open set $\Omega \subset \mathbb{R}^3$ whose boundary $\partial\Omega$ is Lipschitz continuous with a normal $\boldsymbol{n}$ that is defined everywhere. We seek to determine $\mathbf{u}(\Omega, t) : \mathbb{R}^3 \times \mathbb{R} \to \mathsf{L}^2(\Omega)^m = V(\Omega)$ as the solution of a *system of conservation laws*

$$\partial_t \mathbf{u} + \mathbf{div}\,\vec{\mathbf{F}}(\mathbf{u}) = \mathbf{r} \tag{1}$$

Here $\mathbf{div} = (\nabla\cdot\,, \ldots, \nabla\cdot)$ is the vector valued divergence operator and

$$\vec{\mathbf{F}}(\mathbf{u}) = (\boldsymbol{F}_1(\mathbf{u}), \ldots, \boldsymbol{F}_m(\mathbf{u}))$$

is the flux vector with the $i$th component $\boldsymbol{F}_i(\mathbf{u}) : (\mathsf{H}^1(\Omega))^m \to \mathsf{H}(\mathrm{div}, \Omega)$. Function space $\mathsf{H}(\mathrm{div}, \Omega)$ consists of square integrable vector valued functions whose divergence is also square integrable i.e.

$$\mathsf{H}(\mathrm{div}, \Omega) = \{\boldsymbol{v} | \boldsymbol{v} \in \mathsf{L}^2(\Omega)^3,\ \ \nabla\cdot\boldsymbol{v} \in \mathsf{L}^2(\Omega)\}$$

With the aim of constructing a Galerkin form of (1), let

$$(x, y)_\Omega = \int_\Omega xy\,\mathrm{d}v$$

and

$$\langle x, y\rangle_{\partial\Omega} = \int_{\partial\Omega} xy\,\mathrm{d}s$$

denote the standard $\mathsf{L}^2(\Omega)$ and $\mathsf{L}^2(\partial\Omega)$ scalar products respectively. Multiply Equation (1) by a test function $\mathbf{w} \in V(\Omega)$, integrate over $\Omega$ and use the divergence theorem to obtain the following variational formulation:

$$(\partial_t \mathbf{u}, \mathbf{w})_\Omega - (\vec{\mathbf{F}}(\mathbf{u}), \nabla\mathbf{w})_\Omega + \langle\vec{\mathbf{F}}(\mathbf{u})\cdot\boldsymbol{n}, \mathbf{w}\rangle_{\partial\Omega} = (\mathbf{r}, \mathbf{w})_\Omega, \quad \forall\mathbf{w} \in V(\Omega) \tag{2}$$

Finite element methods (FEMs) involve a double discretization. First, the physical domain $\Omega$ is discretized into a collection of $\mathcal{N}_e$ elements

$$\mathcal{T}_e = \bigcup_{e=1}^{\mathcal{N}_e} e \tag{3}$$

 

called a mesh. The function space $V(\Omega)$ containing the solution of (2) is approximated on each element $e$ of the mesh to define a finite-dimensional space $V_e(\mathscr{T}_e)$. With discontinuous finite elements, $V_e$ is a 'broken' function space that consists in the direct sum of elementary approximations $\mathbf{u}_e$ (we use here a polynomial basis $\mathbb{P}^p(e)$ of order $p$):

$$V_e(\mathscr{T}_e) = \{\mathbf{u} | \mathbf{u} \in \mathsf{L}^2(\Omega)^m, \mathbf{u}_e \in \mathbb{P}^p(e)^m = V_e(e)\} \tag{4}$$

Because all approximations are disconnected, we can solve the conservation laws on each element to obtain

$$(\partial_t \mathbf{u}_e, \mathbf{w})_e - (\vec{\mathbf{F}}(\mathbf{u}_e), \nabla \mathbf{w})_e + \langle \mathbf{F}_n, \mathbf{w} \rangle_{\partial e} = (\mathbf{r}, \mathbf{w})_e, \quad \forall \mathbf{w} \in V_e(e) \tag{5}$$

Now, a discontinuous basis implies that the normal trace $\mathbf{F}_n = \vec{\mathbf{F}}(\mathbf{u}) \cdot \boldsymbol{n}$ is not defined on $\partial e$. In this situation, a *numerical flux* $\mathbf{F}_n(\mathbf{u}_e, \mathbf{u}_{e_k})$ is usually used on each portion $\partial e_k$ of $\partial e$ shared by element $e$ and neighbouring element $e_k$. Here, $\mathbf{u}_e$ and $\mathbf{u}_{e_k}$ are the restrictions of solution $\mathbf{u}$, respectively, to element $e$ and element $e_k$. This numerical flux must be continuous, so $\vec{\mathbf{F}} \in \mathsf{H}(\mathrm{div}, \Omega)^m$, and be consistent, so $\mathbf{F}_n(\mathbf{u}, \mathbf{u}) = \vec{\mathbf{F}}(\mathbf{u}) \cdot \boldsymbol{n}$. With such a numerical flux, Equation (5) becomes

$$(\partial_t \mathbf{u}_e, \mathbf{w})_e - (\vec{\mathbf{F}}(\mathbf{u}_e), \nabla \mathbf{w})_e + \sum_{k=1}^{n_e} \langle \mathbf{F}_n(\mathbf{u}_e, \mathbf{u}_{e_k}), \mathbf{w} \rangle_{\partial e_k} = (\mathbf{r}, \mathbf{w})_e, \quad \forall \mathbf{w} \in V_e(e) \tag{6}$$

where $n_e$ is the number of faces of element $e$. Only the normal traces have to be defined on $\partial e_k$ and several operators are possible [21, 22]. It is usual to define the trace as the solution $\mathbf{u}_\mathrm{R}$ of a Riemann problem across $\partial e_k$. We have then $\mathbf{F}_n(\mathbf{u}_e, \mathbf{u}_{e_k}) = \vec{\mathbf{F}}(\mathbf{u}_\mathrm{R}) \cdot \boldsymbol{n}$. Herein, we consider problems with strong shocks [22, 23]. An exact Riemann solver is used to compute the numerical fluxes and a slope limiter [24] is used to produce monotonic solutions when polynomial degrees $p > 0$ are used.

The choice of a basis for $V_e(e)$ is an important issue in constructing an efficient method. Because the field is discontinuous, there is substantial freedom in the selection of the elemental basis. Here, we chose the $\mathsf{L}^2$-orthogonal basis described in Reference [2] as a basis of $P(e)$:

$$P(e) = \{b_1, \ldots, b_k\} \tag{7}$$

where

$$(b_i, b_j)_e = \delta_{i,j}$$

For the time discretization, we use the local time stepping procedure described in Reference [25] that allows to use overall time steps more than 20 times bigger than the classical stability limit of explicit schemes.

## 3. ANISOTROPIC MESH CORRECTION INDICATION

### *3.1. Approach taken*

The goal of the mesh correction indication process is to determine the anisotropic mesh configuration that will most effectively provide the level of accuracy required for the parameters

 

of interest. The literature on error estimation techniques (e.g. References [15, 16]) does provide the mathematical tools and techniques to reliably approach this goal for specific classes of equations under specific limitations on the relationship of the methods to analyse the discretization errors and to improve the mesh. However, these procedures do not yet provide all the ingredients needed for more complex set of equations such as the hyperbolic conservation equations considered here. In particular, the ability to bound the discretization error estimates in appropriate norms and to prove optimal anisotropic mesh configurations is not yet available. On the other hand, it is well recognized that the application of adaptive analysis procedures for these problems yields far superior results to non-adaptive methods. Therefore, the strategy adopted in the present paper is to construct the anisotropic mesh correction indicator in terms of a complete mesh metric field defined over the domain of the analysis and to construct this mesh metric field using a combination of best available methods.

The most direct definition of an anisotropic mesh metric field is one that defines the mapping of an ellipsoid into a unit sphere in terms of a diagonal distortion matrix, where the diagonal terms correspond to the lengths of the principal axes of the ellipsoid, times a rotation matrix that accounts for the orientation of the ellipsoid. When used for constructing the anisotropic mesh size field, lengths of the principal axes are interpreted as the desired mesh edge lengths at that location.

$$Q(x, y, z) = \underbrace{\begin{bmatrix} 1/h_1 & 0 & 0 \\ 0 & 1/h_2 & 0 \\ 0 & 0 & 1/h_3 \end{bmatrix}}_{\text{distortion}} \cdot \underbrace{\begin{bmatrix} \boldsymbol{e}_1 \\ \boldsymbol{e}_2 \\ \boldsymbol{e}_3 \end{bmatrix}}_{\text{rotation}} \tag{8}$$

where $\boldsymbol{e}_1$, $\boldsymbol{e}_2$, $\boldsymbol{e}_3$ are orthogonal unit vectors associated with the principal axes of the ellipsoid at point $(x, y, z)$, and $h_1, h_2, h_3$ are the desired mesh edge lengths along these three axes.

To date the most common approach to the definition of the mesh metric field for adaptive mesh construction is to relate it to the Hessian of an appropriate solution variable $u$ [4, 6, 12]:

$$H(u) = \begin{bmatrix} \dfrac{\partial^2 u}{\partial x^2} & \dfrac{\partial^2 u}{\partial x \partial y} & \dfrac{\partial^2 u}{\partial x \partial z} \\ \dfrac{\partial^2 u}{\partial y \partial x} & \dfrac{\partial^2 u}{\partial y^2} & \dfrac{\partial^2 u}{\partial y \partial z} \\ \dfrac{\partial^2 u}{\partial z \partial x} & \dfrac{\partial^2 u}{\partial z \partial y} & \dfrac{\partial^2 u}{\partial z^2} \end{bmatrix} \tag{9}$$

and construct $Q(x, y, z)$ by decomposing, scaling $H(u)$ and bounding the maximum desired mesh edge lengths:

$$Q(x, y, z) = \begin{bmatrix} \sqrt{\lambda_1'} & 0 & 0 \\ 0 & \sqrt{\lambda_2'} & 0 \\ 0 & 0 & \sqrt{\lambda_3'} \end{bmatrix} \cdot \begin{bmatrix} \boldsymbol{e}_1 \\ \boldsymbol{e}_2 \\ \boldsymbol{e}_3 \end{bmatrix} \tag{10}$$

 

with

$$\lambda_i' = \max\left(\phi(x, y, z)|\lambda_i|, \frac{1}{h_{\max}^2}\right) \quad \forall i \in (1, 2, 3) \tag{11}$$

where

- $|\lambda_i|$ is the $i$th absolute eigenvalue of the Hessian matrix $H$;
- $\boldsymbol{e}_i$ is the $i$th unit eigenvector of $H$;
- $\phi(x, y, z)$ is a scale factor at point $(x, y, z)$, determined in terms of an error estimate/indicator (e.g. leading element interpolation error) to equilibrate the distribution of the error;
- $h_{\max}$ is user defined maximal allowable mesh edge length in the mesh. Since Hessian $H(u)$ can be singular, it is needed to apply $h_{\max}$ in case $\lambda_i$ is zero or close to zero.

A variety of arguments have been given as to the rationale for using the second derivative information of the Hessian matrix in the construction of the anisotropic mesh metric field. The most compelling one is to consider basic interpolation theory coupled with an equivalence of norm argument to show the error in the interpolant is equivalent to a norm of interest for the finite element methods. In the simplest possible terms, the error in a polynomial interpolant is proportional to the derivatives of order equal to the first order polynomial interpolant cannot exactly represent. In the case where piecewise linear finite elements are used, the interpolation error is proportional to second derivatives. Kunert [8] provides some degree of analysis of the use of the Hessian matrix anisotropic in adaptive analysis including pointing some of the critical limitations of its use. The analysis by Rachowicz [11] focuses on the $\mathsf{L}^2$ error norm for interpolation on an anisotropic mesh showing that the error is associated with the $p+1$ derivatives for a $p$th order interpolant. He further relates this error to an $\mathsf{H}^1$-seminorm of the finite element solution for the specific case of parallelogram elements [26] in which case the dominent error term is associated with error is associated with the $p+1$ derivatives when the solution is of sufficient smoothness.

Since the examples presented in this paper are based on piecewise linear $\mathsf{L}^2$ discontinuous finite elements, the Hessian matrix will be employed as a key ingredient in the construction of the mesh metric field in the regions where the solution is smooth. Specific care must be exercized in the definition of this mesh metric field. The most obvious concern is the ability to calculate values to the second derivatives of a discontinuous field. One approach used with $C^0$ finite element basis is the construction of a 'recovered' Hessian [3] using patchwise projection procedures in a manner similar to that used to define the popular Zienkiewicz–Zhu error estimators [27]. Although it may be possible to use a similar approach here, the discontinuous nature of the DG basis makes it questionable. Therefore, the present work employs the reconstruction procedure of Section 3.2 to evaluate the Hessian matrix in the portions of the domains where the exact solution is assumed to be smooth.

Since the procedure will be applied to the adaptive solution of transient flow problems that contain solution discontinuities (shocks, contact discontinuities and expansion waves), care must be taken in the construction of the mesh metric field. Clearly, it is inappropriate to construct and employ the Hessian matrix in the immediate vicinity of the discontinuities, the locations of which are not known *a priori* and which move as the transient solution evolves. Therefore, a two step procedure is used to construct the mesh metric field around discontinuities. We first determine the location of the elements crossing discontinuities using

 

the solution smoothness indicator presented in Section 3.3. Then, we define the mesh metric field along the discontinuities using the procedure given in Section 3.4.

Mesh metric fields are constructed here using solutions of compressible flows. The structure of such flows is usually formed of very smooth regions separated by discontinuities (waves). Hessians based on such solutions will generate metric fields with brutal variations of mesh sizes. In Section 3.5, we will indicate how the mesh metric fields over the various portions of the domain are smoothed to produce the final mesh metric field used by the mesh adaptation procedures. The development of an efficient smoothing procedure of the anisotropic metric was a crucial step in the whole process of adaptation.

### *3.2. Calculation of Hessian matrix from discontinuous fields*

In this paper, we only consider piecewise linear polynomial approximations. For computing the Hessian of $\rho(x_n, y_n, z_n)$ at each vertex $n$ of co-ordinates $x_n, y_n, z_n$, we proceed in two steps. We first reconstruct a linear approximation

$$\rho(x, y, z) = \alpha_1^n + \alpha_1^n(x - x_n) + \alpha_2^n(y - y_n) + \alpha_3^n(z - z_n)$$

of $\rho$ around each vertex $n$ using the average values $\rho_i$ at each centroid $(x_m, y_m, z_m)$ of the $N_e$ neighbouring elements of vertex $i$:

$$\rho(x_i, y_i, z_i) = \alpha_1^n + \alpha_2^n(x_i - x_n) + \alpha_3^n(y_i - y_n) + \alpha_4^n(z_i - z_n) \quad i = 1, \ldots, N_e$$

This system of $N_e$ equations with four unknowns is solved using normal equations (least squares). Then, we reconstruct the three derivatives:

$$\left.\frac{\partial \rho}{\partial x}\right|_n = a_1^n + a_2^n(x - x_n) + a_3^n(y - y_n) + a_4^n(z - z_n)$$

$$\left.\frac{\partial \rho}{\partial y}\right|_n = b_1^n + b_2^n(x - x_n) + b_3^n(y - y_n) + b_4^n(z - z_n)$$

$$\left.\frac{\partial \rho}{\partial z}\right|_n = c_1^n + c_2^n(x - x_n) + c_3^n(y - y_n) + c_4^n(z - z_n)$$

using the previously reconstructed nodal gradients $\alpha_n^j$. From these results, Hessian computation is straightforward. We have, for example then

$$\frac{\partial^2 \rho}{\partial x^2} = a_2^n, \quad \frac{\partial^2 \rho}{\partial y^2} = b_3^n$$

or

$$\frac{\partial^2 \rho}{\partial x \partial y} = \frac{1}{2}(a_3^n + b_2^n)$$

 

### *3.3. Isolation of discontinuities using a smoothness indicator*

The main challenge of solving hyperbolic problems such as compressible gas dynamics is that the solutions is able to develop discontinuities in finite time even for smooth initial data. It has been shown [28] that only schemes that are of first order of accuracy are able to produce monotonic solutions when discontinuities are present. First order schemes produce too much numerical dissipation and do not exhibit the required resolution for convection dominated problems (i.e. problems with small physical dissipation).

The spurious oscillations produced near discontinuities by a higher order method such as the DGM may amplify in time (especially near shocks) and cause the solution to become unbounded. It is crucial to be able to control and eliminate the spurious oscillations introduced by higher order schemes.

Procedures to suppress oscillations near discontinuities are called limiters [29–32]. Limiters tend to reduce the accuracy of solutions to first order where they are applied. With an adaptive strategy, discontinuities are captured by reducing element sizes at their vicinity accounting for alignment with the discontinuity and directional variation differences in local solution information. The limiter is only applied in the one or two layers of elements crossing discontinuities.

We introduce here a procedure that allows us to detect discontinuities. Consider element $e$ of boundary $\partial e$. Solving the DGM implies the computation of a numerical flux $\mathbf{F}_n(\mathbf{u}_e, \mathbf{u}_{e_k}) = \vec{\mathbf{F}}(\mathbf{u}_\mathrm{R}) \cdot \boldsymbol{n}$ (cf. Section 2) where $\mathbf{u}_\mathrm{R}$ is the solution of the Riemann problem at the boundary of the element $\partial e$. If $\mathbf{u}_{ex}$ is the exact solution of (1) and $h_e$ is the size of element $e$ (e.g. the radius of the circumsphere of a tetrahedron) it has been proven in Reference [33] that the following result holds:[‡]

$$\frac{1}{|\partial e|}\int_{\partial e}(\mathbf{u}_\mathrm{R} - \mathbf{u}_{ex})\,\mathrm{d}s = \mathcal{O}(h_e^{2p+1}) \tag{12}$$

The super-convergence result (12) implies that the solution $\mathbf{u}_\mathrm{R}$ of the Riemann problem at element interfaces is, in average, much closer to the exact solution than elementary solution $\mathbf{u}_e$. For linear problems, the solution of the Riemann problem is the upwind value of $\mathbf{u}_e$ at boundary $\partial e$. On one element $e$, the downwind values (i.e. the upwind values of the next element) are the ones which are super-convergent.[§]

We consider the following elemental quantity:

$$I_e = \int_{\partial e}(\mathbf{u}_e - \mathbf{u}_\mathrm{R})\,\mathrm{d}s = \int_{\partial e}(\mathbf{u}_e - \mathbf{u}_{ex})\,\mathrm{d}s + \int_{\partial e}(\mathbf{u}_{ex} - \mathbf{u}_\mathrm{R})\,\mathrm{d}s \tag{13}$$

Due to the superconvergence result (12), the second integral is $\mathcal{O}(h^{2(p+1)})$ while the first is $\mathcal{O}(h^{p+2})$. Thus, $I_e = \mathcal{O}(h^{p+2})$ across edges (2D case) or faces (3D case) where the solution is smooth. If $\mathbf{u}$ is discontinuous in the immediate vicinity of $\partial e$, then either or both of $\mathbf{u}_{ex} - \mathbf{u}_e$

[‡]This result was proven in the case of linear problems and was tested successfully on a non-linear Burgers equation.

[§]We claim here the following conjecture about this superconvergence result: the convergence of the solution at downwind is necessary for the DGM to produce convergent result. If this result was not holding, truncation errors would propagate along characteristics of the flow.

 

and $\mathbf{u}_{ex} - \mathbf{u}_{\mathrm{R}}$ are $\mathcal{O}(1)$; hence,

$$I_e = C \begin{cases} h^{p+2} & \text{if } \mathbf{u}|_{\partial e} \text{ is smooth} \\ h & \text{if } \mathbf{u}|_{\partial e} \text{ is discontinuous} \end{cases} \tag{14}$$

We construct a discontinuity detector by normalizing $I_e$ relative to an 'average' $\mathcal{O}(h^{(p+1)/2})$ convergence rate and the solution on $e$ to obtain

$$\mathscr{I}_e = \frac{\left|\int_{\partial e}(\mathbf{u} - \mathbf{u}_{\mathrm{R}})\,\mathrm{d}s\right|}{h^{(p+1)/2}|\partial e|\|\mathbf{u}\|} \tag{15}$$

In examples, we choose $h_e$ as the radius of the circumscribed circle in element $e$, and use a maximum norm based on local solution maxima at integration points in two dimensions and an element average in one dimension. We have then

$$\mathscr{I}_e = C \begin{cases} h^{(p+1)/2} & \text{if } \mathbf{u}|_{\partial e} \text{ is smooth} \\ h^{-(p+1)/2} & \text{if } \mathbf{u}|_{\partial e} \text{ is discontinuous} \end{cases} \tag{16}$$

Consequently, $\mathscr{I}_e \to 0$ as either $h \to 0$ or $p \to \infty$ in smooth solution regions, whereas $\mathscr{I}_e \to \infty$ near a discontinuity. Thus, the discontinuity detection scheme is

$$\begin{cases} \text{if } \mathscr{I}_e > 1, & \mathbf{u} \text{ is discontinuous} \\ \text{if } \mathscr{I}_e < 1, & \mathbf{u} \text{ is smooth} \end{cases} \tag{17}$$

### *3.4. Anisotropic mesh construction across jump features*

In portions of domain across discontinuities, we have shown in Section 3.3 that the discontinuities can be detected to provide useful information for an adaptive process. Due to the discontinuities, the element discretization error cannot be controlled (i.e. bounded) in elements crossing a discontinuity in the classic sense.

Let us consider the following function:

$$\mathscr{H}(x, \alpha) = \left(\frac{1}{2} + \frac{\tan^{-1}(\alpha x)}{\pi}\right) \tag{18}$$

that models a discontinuous function with a jump of 1 at $x = 0$. At the limit $\lim_{\alpha\to\infty}$, $\mathscr{H}$ tends to the Heaviside function. The second order derivative of (18) gives

$$\frac{\partial^2 \mathscr{H}(x, \alpha)}{\partial x^2} = \frac{2\alpha^2 x}{(1 + (\alpha x)^2)^2 \pi} \tag{19}$$

If we take $\alpha$ bounded in (18), we obtain a function that approximates the discontinuity with the same kind of behaviour as a DGM numerical solution. The second order derivative (19) is then equal to 0 at $x = 0$, going from large positive values for $x < 0$ to large negative values at $x > 0$ (see Figure 1).

Numerical Hessians in elements crossing the discontinuity are highly ill conditioned and cannot be used: across a shock of direction $\boldsymbol{n}$, $\partial^2 u/\partial n^2 = \boldsymbol{n} \cdot H \cdot \boldsymbol{n}$ changes sign (see Figure 1). Its value is numerically undertermined in terms of sign and amplitude. In elements where

 

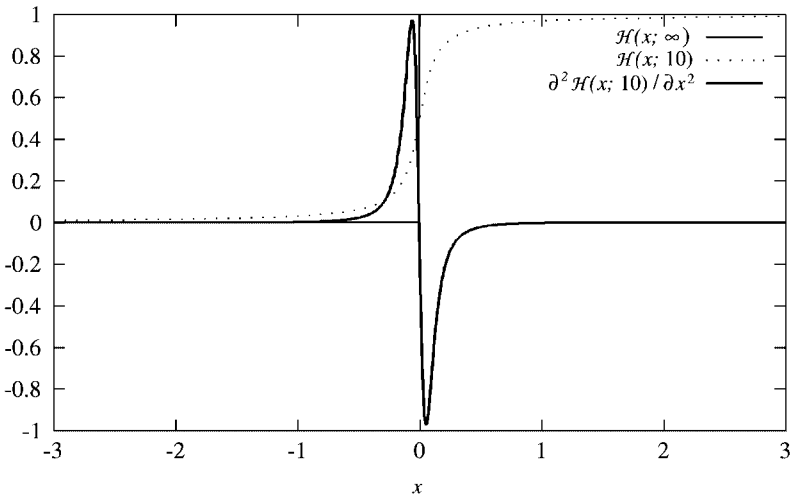


Figure 1. Illustration of the behaviour of numerical second derivatives through discontinuities.

we have detected a discontinuity, we found it better to use the gradient $\boldsymbol{n} = \nabla w/|\nabla w|$ for determining the direction of the shock. The gradient of $u$ is high everywhere through the shock and has a constant sign. It is then much better conditioned. The resulting adaptive strategy can be described as follows:

- Determine the elements that cross a discontinuity using (17);
- In elements where the solution is smooth, use (10) and (11) to construct an anisotropic metric field;
- In elements where the solution is discontinuous, use the reconstructed gradients to compute the normal direction $\boldsymbol{n}$ to the discontinuity. Then, build up a spheroidal metric by selecting $\lambda_1' = 1/h_{\min}^2$ in the normal direction and $\lambda_2' = \lambda_3' = 1/h_{nbr}^2$ in the two tangential directions. Here, $h_{\min}$ is user defined minimal allowed edge length in the mesh. Since the solution is continuous in tangential directions of discontinuity, we choose

$$h_{nbr} = \frac{h^{\boldsymbol{n}+} + h^{\boldsymbol{n}-}}{2} \tag{20}$$

  where $h^{\boldsymbol{n}+}$ and $h^{\boldsymbol{n}-}$ is the mesh size along tangential directions in nearby smooth regions on both sides of the discontinuity;
- When a metric field has been computed both in smooth and discontinuous regions, smooth this metric field to reconnect the anisotropic mesh metric field to be used by the mesh adaptation procedure. The concepts of metric smoothing is outlined in Section 3.5. Details can be found in Reference [34].

### *3.5. Smoothing of mesh metric field*

In order to smooth a piecewise linearly interpolated mesh metric field respecting existing anisotropy, let us consider two adjacent points where arbitrary mesh metrics are specified (Figure 2). We are interested in adjusting the two mesh metrics so that physical anisotropy is

 

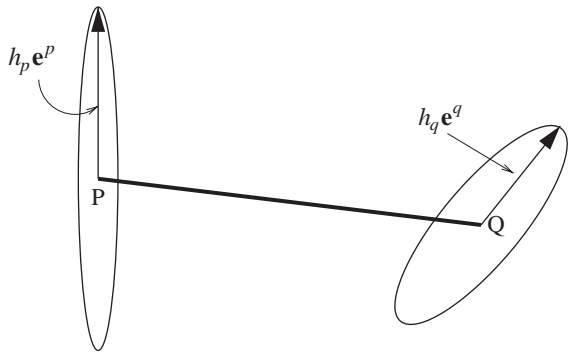


Figure 2. Illustration to anisotropy respect factor and directional H-shock. $P$ and $Q$ are two adjacent points with mesh metric specified (indicated by the two ellipses). $\mathbf{e}^p$ and $\mathbf{e}^q$ show an eigenvector for each metric. $h_p$ and $h_q$ indicate the desired edge length along $\mathbf{e}^p$ and $\mathbf{e}^q$.

respected with direction and size both change smoothly from $P$ to $Q$. Two useful definitions, anisotropy respect factor and directional H-shock, have been used.

*Definition*
The anisotropy respect factor related to points $P$ and $Q$ is of the value

$$\alpha = \frac{(R_q - 1)R_p}{(R_p - 1)R_q} \quad (R_p \geqslant R_q) \tag{21}$$

where $R_p$, $R_q$ are the aspect ratio of the mesh metric at points $P$ and $Q$, respectively. The aspect ratio $R$ of a mesh metric is the ratio of the maximal desired edge length to the minimal desired length.

The motivation of introducing $\alpha$ is to smooth directional variation between two adjacent points. Equation (22) gives a method to correct eigenvectors of the less anisotropic mesh metric based on $\alpha$, which ensures to respect the mesh metric with strong anisotropy and respect both in case $R_p = R_q$.

$$\mathbf{e}_i^q|_{\text{new}} = (1-\alpha)\mathbf{e}_j^p + \alpha\mathbf{e}_i^q \quad (i, j = 1, 2, 3) \tag{22}$$

where $R_p \geqslant R_q$, $\mathbf{e}_i^q$ is an eigenvector of the mesh metric at point $Q$, $\mathbf{e}_i^q|_{\text{new}}$ is the corrected one, and $\mathbf{e}_j^p$ is the eigenvector associated with $\mathbf{e}_i^q$ at point $P$.

*Definition*
The directional H-shock related to points $P$ and $Q$ associated with eigenvector pair $(\mathbf{e}^p, \mathbf{e}^q)$ is of the value

$$\max\left(\frac{h_p}{h_q}, \frac{h_q}{h_p}\right)^{1/L'(PQ)} \tag{23}$$

with $h_p$, $h_q$ be the desired length along direction $\mathbf{e}^p$ and $\mathbf{e}^q$ at points $P$ and $Q$, respectively, and $L'(PQ)$ be the length of segment $PQ$ with respect to the mesh metric variation over $PQ$ (refer to (24) in Section 4.1).

 

This H-shock measures the direction-related desired edge length variation between two mesh metrics. In particularly, it represents the progression ratio when fitting the mesh metric variation over $PQ$ with a sequence of edges in geometric progression.

The anisotropic smoothing procedure modifies a piecewise linear field with mesh metrics attached to vertices. It repeatedly processes the edges of the mesh to adjust the mesh metrics at end vertices in terms of Equations (22) and (23) until the directional H-shocks associated with all edges are bounded by a given value $\beta$.

## 4. ANISOTROPIC MESH ADAPTATION VIA LOCAL MESH MODIFICATION

Given the mesh metric field defined over the domain, local mesh modification is applied to yield the desired anisotropic mesh. Next to the application of mesh modification is the ability to use the local mesh and the mesh metric field to quickly determine the appropriate mesh modification to apply. This section outlines the mesh modification that are used to convert the given mesh into one that satisfies the given mesh metric field [35, 36].

Mesh modification operators include entity (i) split, (ii) collapse, (iii) swap and (iv) reposition. For purposes of anisotropic mesh adaptation, mesh modification is used to directionally refine and coarsen the mesh, and to realign the mesh in order to satisfy the given anisotropic mesh metric field.

### *4.1. Mesh modification criteria*

Since the anisotropic mesh size field represents the transformation that map an ellipsoid into a unit sphere, the idea tetrahedron that satisfies the mesh size field should be mapped into a unit equilateral tetrahedron in the transformed space. Figure 3 demonstrates this concept. The left figure depicts two desired anisotropic tetrahedra in physical space, while the transformation associated with the mesh metric field is indicated by the two matrices. As illustrated by the right

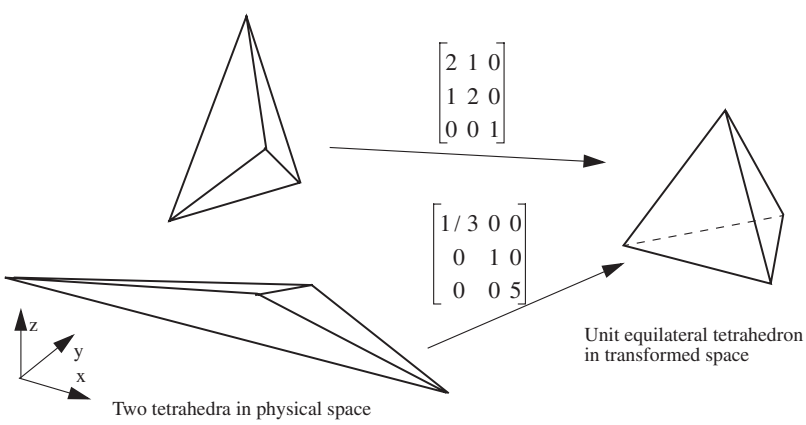


Figure 3. Desired tetrahedra are mapped into unit equilateral tetrahedra by the transformation mesh metric defines.

 

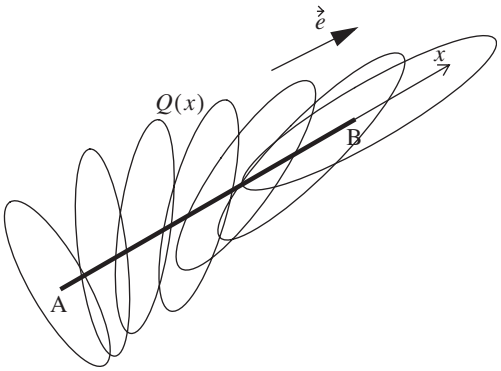


Figure 4. Illustration of length computation in transformed space. Ellipses indicate $Q(x)$ defined over edge $AB$.

figure, both tetrahedra are transformed into a unit equilateral tetrahedron by their corresponding transformation matrix.

To make any given mesh satisfying the given mesh size field by mesh modifications, we take philosophy as follows:

- identify those mesh entities not satisfying the mesh size field;
- perform appropriate mesh modifications so that local mesh will better satisfy the mesh size field;
- repeat above steps until the mesh size field is satisfied to an acceptable degree.

The degree of the satisfaction of a mesh to a mesh size field can be measured by mesh edge length in the transformed space. Consider mesh edge $AB$ and the transformation representation of the mesh size field $Q(x)$ over $AB$ (refer to Figure 4). In general, the length of $PQ$ in transformed space can be computed by [6, 35, 37]

$$L'(AB) = \int_A^B \sqrt{\boldsymbol{e} \cdot Q(x)Q(x)^{\mathrm{T}} \cdot \boldsymbol{e}^{\mathrm{T}}}\,\mathrm{d}x \tag{24}$$

where $\boldsymbol{e}$ is the unit vector associated with edge $AB$ in the physical space.

Since it is not possible to ensure that all mesh edges exactly match the requested lengths, the goal of mesh modifications is to make the transformed length of all mesh edges fall into an interval close to one. Particularly, we choose interval [0.5, 1.4] in the examples given in Section 5 which is large enough to avoid oscillations [35, 36].

Sliver tetrahedra (poorly shaped tetrahedra not bounded by any short mesh edge in transformed space) may exist even if the edge length criteria is met, so an additional criteria is needed to determine and eliminate sliver tetrahedra. One of the standard non-dimensional shape measure, the cubic of mean ratio [38] in the transformed space, is used for this purpose. Let $Q$ be the associated transformation matrix of the tetrahedron,[¶] the cubic of mean ratio in

[¶]In case the transformation is not constant over the tetrahedron, the one with maximum aspect ratio is considered as associated transformation.

 

transformed space, $\eta'$, is

$$\eta' = \frac{15552(|Q|V)^2}{(\sum_{i=1}^{6} \boldsymbol{l}_i \cdot QQ^{\mathrm{T}} \cdot \boldsymbol{l}_i{}^{\mathrm{T}})^3} \tag{25}$$

where $|Q|V$ is the volume of the tetrahedron in the transformed space ($|Q|$ represents the determinant of the transformation, $V$ is the volume of a tetrahedron in physical space), and $\boldsymbol{l}_i$ $(i = 1..6)$ are vectors associated with the six edges of the tetrahedron. Note that $\eta'$ has been normalized to interval $[0, 1]$ with 0 for flat tetrahedron and 1 for equilateral tetrahedron in transformed space. In Section 4.4, all tetrahedra with $\eta'$ less than a given threshold are eliminated through mesh modifications.

### *4.2. Refinement*

In three dimensions, edge, face and region split operators can be used to refine the mesh [39–42]. The set of predefined patterns described in Reference [41] are used here to refine the mesh since it is efficient (linear complexity), prevents over-refinement and provide possibilities to maintain or even improve mesh quality [35, 36].

### *4.3. Coarsening*

Edge, face, and region collapse operations can be defined in an analogous way to the split operations and can be used for mesh coarsening. The edge collapse tends to be the most useful approach, however the other operations have been found of use in specific cases [35, 36]. In case a short edge is adjacent to a long edge, repositioning the common vertex of both edges can also be a useful approach.

The coarsening algorithm first determines a list of vertices that bound short edges, then eliminates them in the order of topologically every other vertex. Consider a mesh vertex that bounds at least a short mesh edge, the coarsening process first get its shortest adjacent mesh edge, and evaluate the removal of this vertex by collapsing it onto the vertex at the other end of the shortest edge. If this collapsing will create long mesh edges in transformed space, repositioning this vertex will be evaluated. If edge collapse is geometrically not acceptable, consideration is given to compound operators to first attempt a swap operation which would allow the desired collapse to be applied.

To prevent the possible oscillation between refining and collapsing, any of above local mesh modifications is considered unacceptable if it creates a long mesh edge in transformed space.

### *4.4. Re-alignment*

Local mesh modifications, particularly edge and face swap operators, can be used to improve the quality of the mesh by replacing poorly shaped elements with higher quality elements [10, 41, 43].

The re-alignment algorithm aims at eliminating existing sliver tetrahedra in the transformed space. To support the intelligent determination of local mesh modifications, it is useful to classify sliver tetrahedra into two types (refer to Figure 5). A tetrahedron is classified as type I sliver if two opposite edges of the tetrahedron almost intersect; a tetrahedron is classified as type II if one vertex of the tetrahedron is close to the centroid of its opposite face.

 

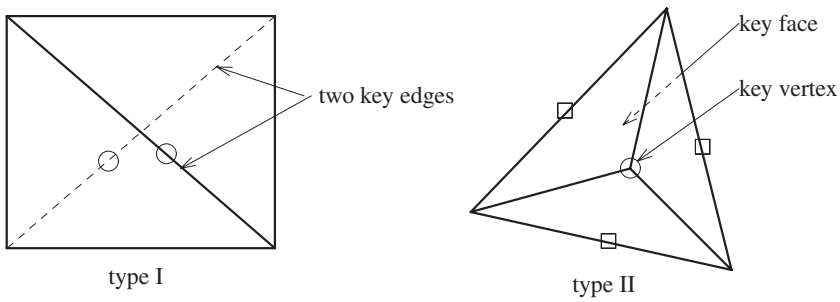


Figure 5. Sliver tetrahedron types and associated key entities.

Table I. Determination of local mesh modifications.

| Priority | Mesh modifications for type I | Mesh modifications for type II |
|---|---|---|
| 1 | Swap either key mesh edge | Swap the key face or relocate the key vertex |
| 2 | Split either key edge and relocate the new vertex, split both edges and collapse the interior edge | Split the face then split/relocate the new vertex, swap the three edges that bound the face |
| 3 | Relocate vertices of the tetrahedron | Relocate the three vertices that bound the face |

Key mesh entities to eliminate the sliver tetrahedron can be identified for these two types: in case of type I, it is a pair of mesh edges (indicated by circles); In case of type II, it is a mesh face (indicated by the three squares) and a mesh vertex (indicated by the circle). Table I lists the promising local mesh modification operation(s) to be evaluated for each type. To be effective, mesh modifications are evaluated at three priority levels.

## 5. RESULTS

### *5.1. Acoustic pulse*

The propagation of sound waves in the air is governed by the linearized Euler equations of fluid dynamics. They can be written, in two dimensions:

$$\frac{\partial}{\partial t}\begin{bmatrix} P \\ u \\ v \end{bmatrix} + \frac{\partial}{\partial x}\begin{bmatrix} \rho_0 c^2 u + u_0 P \\ P/\rho_0 + u_0 u \\ u_0 v \end{bmatrix} + \frac{\partial}{\partial y}\begin{bmatrix} \rho_0 c^2 v + v_0 P \\ v_0 y \\ P/\rho_0 + v_0 v \end{bmatrix} = \mathbf{0} \tag{26}$$

where $\rho_0$ is the unperturbated density of the fluid, $u_0$ and $v_0$ are the two components of the mean flow $\boldsymbol{v}_0$, $c_0$ is the sound speed, $P$ is a perturbation of the pressure and $\boldsymbol{v}$ is the perturbation of the velocity of components $u$ and $v$.

We solve (26) using the DGM with a numerical flux that is the exact solution of an associated one-dimensional Riemann problem. The Riemann problem consist in finding the self similar

 

solution of a hyperbolic problem with discontinuous initial data. We consider an interface of normal $\boldsymbol{n}$ that separates 2 constant states $P_l, v_{nl}, v_{tl}$ and $P_r, v_{nr}, v_{tr}$. At $t = 0$, we impulsively remove the interface. If we suppose that the mean flow $\boldsymbol{v}_0$ is subsonic everywhere i.e. $|\boldsymbol{v}_0| < c_0$ everywhere, the solution of the Riemann problem can be written as a superposition of three waves, the first one moving at positive speed $v_{n0} + c_0$, one moving at negative speed $v_{n0} - c_0$ and the last one moving at speed $v_{n0}$.

The solution $P, \boldsymbol{v}$ for all times $t$ at $-ct < x < ct$ consists in the superposition of the characteristic variables:

$$P_l/(\rho_0 c_0) + v_{nl} = P/(\rho_0 c_0) + v_n$$

$$P_r/(\rho_0 c_0) - v_{nr} = P/(\rho_0 c_0) - v_n$$

Solution of the Riemann problem is then

$$P = \underbrace{\frac{p_l + p_r}{2}}_{\{P\}} + \rho_0 c_0 \underbrace{\frac{v_{nl} - v_{nr}}{2}}_{[\![v_n]\!]}$$

$$v_n = \underbrace{\frac{v_{nl} + v_{nr}}{2}}_{\{v_n\}} + \frac{1}{\rho_0 c_0} \underbrace{\frac{P_l - P_r}{2}}_{[\![P]\!]}$$

$$v_t = \underbrace{\frac{v_{tl} + v_{tr}}{2}}_{\{v_t\}} + \mathrm{sign}(v_{n0}) \underbrace{\frac{v_{tl} - v_{tr}}{2}}_{[\![v_t]\!]}$$

Three exact solutions of the linearized Euler equations may be found in Reference [44]. The first one is the expansion of an initial axisymmetric pressure pulse in a constant mean flow. The initial pulse is Gaussian:

$$P(0, \mathbf{x}) = \varepsilon_1 \mathrm{e}^{-\alpha_1 \mathbf{x}^2}$$

with the Gaussian amplitude $\varepsilon_1 = 0.01$, the Gaussian half width $h_1 = 10$ and $\alpha_1 = \log(2)/h_1^2$. The domain of computation is a square of dimensions $400 \times 400$ centred at the origin. We have performed one computation using an initial unstructured triangular mesh. The mesh was adapted at $t = 0$ in order to adapt the steep initial conditions. This example has been chosen because it has a non-trivial analytical solution, with waves of known speed.

Figure 6 shows meshes and pressure contours for the acoustic pulse problem. Physical parameters for this run were $c_0 = 1$, $\rho_0 = 1.225$ and $\boldsymbol{v}_0$ a Mach 0.5 constant field going from left to right. The mesh was adapted every second and minimal and maximal allowed mesh sizes were chosen as $h_{\min} = 0.5$ and $h_{\max} = 50$. At $t = 150$, 151 mesh adaptation were performed, including the one at $t = 0$. Figure 6 shows that the adaptive procedure is able to track accurately wave fronts: iso-contours remain axisymmetrical and smooth at all times. Note that the anisotropic procedure was not able to produce elongated elements at early times because the radius of curvature of the wave front is small. It is only at later stages that anisotropic elements were created.

 

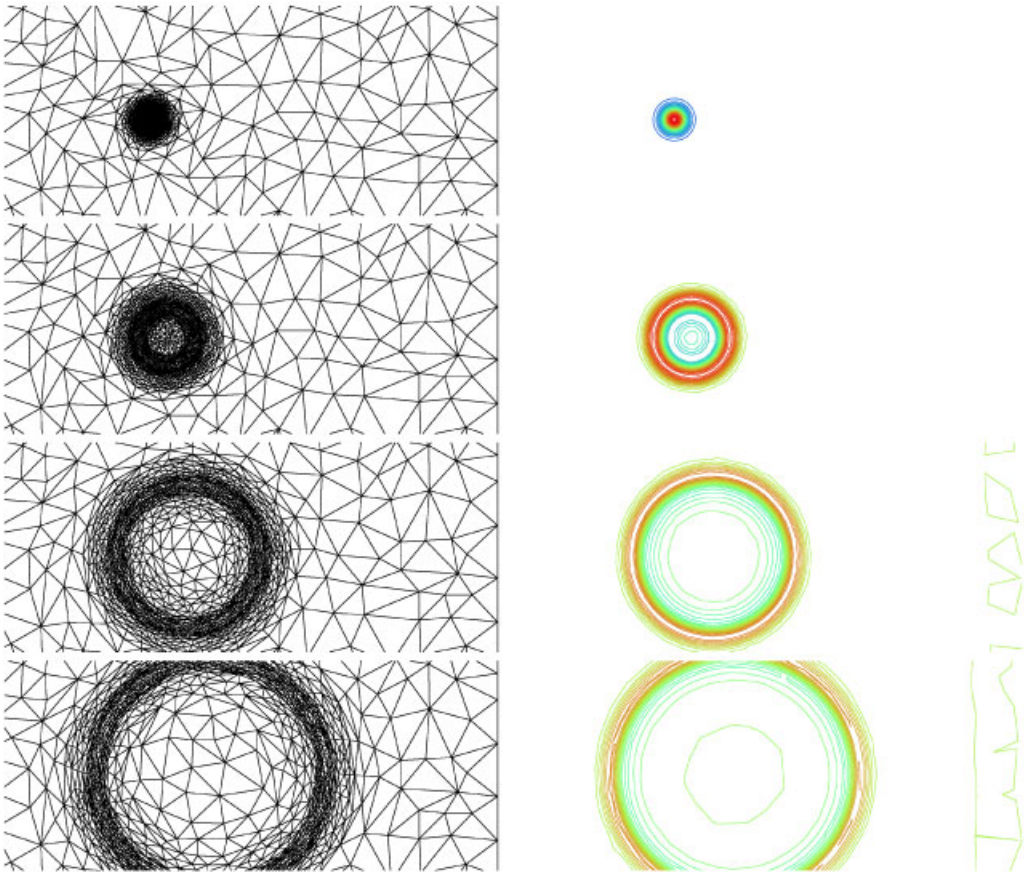

Figure 6. Meshes (left) and pressure contours (right) for the acoustic pulse problem at times $t = 0{,}50,\ 100$ and $150$.

Neverthless, it is still difficult to assert that the adaptive procedure is able to predict accurately the right wave speeds. For that, we have plotted the pressure along the $x$ axis and compare it with the analytical solution (Figure 7).

Figure 6 compares the exact solution with the adaptive DGM computation. Both curves are so well superimposed that it is difficult to differentiate them. This shows clearly that the adaptive procedure correctly predicts the wave speeds but it also shows that the numerical diffusion introduced by the numerous adaptations (151 adaptations at $t = 150$) is small.

### 5.2. *Cannon blast problem*

In this section, we will present the results of some compressible inviscid flow problems involving the solution of the Euler equations [28] by a DG method. The three-dimensional Euler equations

 

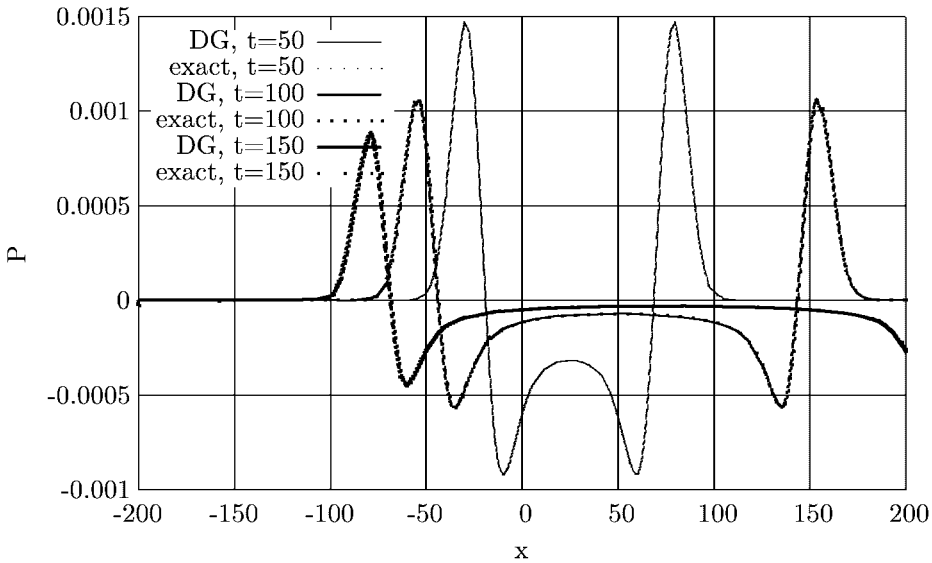


Figure 7. Pressure plots along $x$ axis of exact solution and numerical solution at different times.

can be written as

$$\frac{\partial}{\partial t}\begin{bmatrix}\rho\\ \rho u\\ \rho v\\ \rho w\\ \rho E\end{bmatrix}+\frac{\partial}{\partial x}\begin{bmatrix}\rho u\\ \rho u^2+P\\ \rho u\ v\\ \rho u\ w\\ (\rho E+P)u\end{bmatrix}+\frac{\partial}{\partial y}\begin{bmatrix}\rho v\\ \rho u\ v\\ \rho v^2+P\\ \rho v\ w\\ (\rho E+P)v\end{bmatrix}+\frac{\partial}{\partial z}\begin{bmatrix}\rho u\\ \rho u\ w\\ \rho v\ w\\ \rho w^2+P\\ (\rho E+P)w\end{bmatrix}=\mathbf{0} \tag{27}$$

Here $\rho$ is the fluid density, $\boldsymbol{v}$ the velocity with components $u$, $v$ and $w$, $E$ the internal energy, $P$ the pressure. An equation of state of the form $P = P(\rho, E)$ is also necessary to close the system. The DG method and the associated software [2] may be used for any equation of state which only enters the numerical method through the calculation of the numerical flux. Here, we have chosen the perfect gas equation of state

$$P = (\gamma - 1)\rho\left[E - \frac{\|\boldsymbol{v}\|^2}{2}\right] \tag{28}$$

with the gas constant $\gamma = 1.4$.

Consider the problem of a 2D perforated tube of diameter 155 mm (a section of a cannon). The diameter of the perforated holes inside the barrel (the muzzle break) are $d = 28.6$ mm.

The initial conditions for the problem are the one of a shock tube. We consider a virtual interface inside the barrel (see mesh refinement for $t = 0$ at Figure 8). The initial pressure for the gas inside of the tube are $P = 57,273,627.96$ Pa i.e. more than 500 times the external atmospheric pressure of $P_{\text{atm}} = 101,300$ Pa. The initial temperature of the air inside the tube is $T = 2111.5$ K and its initial velocity along $x$ direction is 0.

 

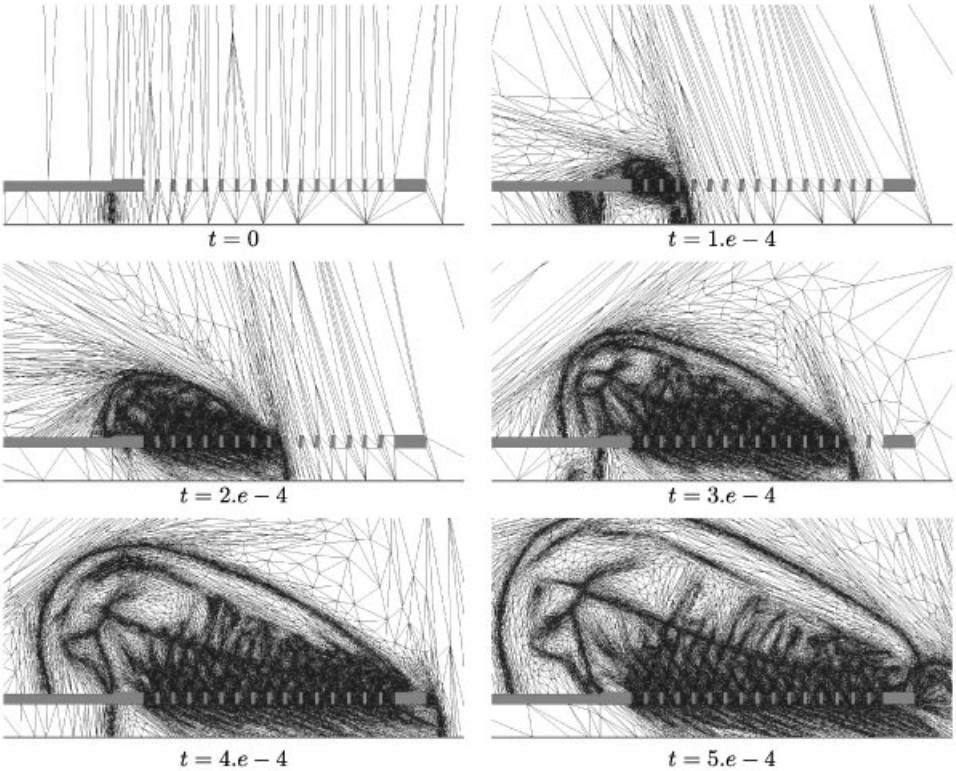


Figure 8. Evolution of the adapted meshes for the cannon blast problem.

The final time of the computation was $t_{\text{end}} = 5 \times 10^{-4}$ s. A second order Runge–Kutta time integration scheme was used. The time steps were computed adaptively with a CFL limit of 1.0. Starting time steps were about $5 \times 10^{-8}$ s and the final time steps were about $1.5 \times 10^{-8}$ s. The mesh was refined every $10^{-6}$ s so that the total number of mesh refinements is 501, including the initial refinement that enables the correct capture of the initial discontinuous state (see Figure 8). The total number of solution time steps is 45 438. The total number of degrees of freedom for this problem starts at 5556 which corresponds to 463 triangles. After the 501 adaptations, the number of degrees of freedom reaches 778 488 which corresponds to 64 874 triangles. Figure 8 show the evolution of the mesh for the cannon blast problem. The minimum mesh size allowed for this problem was $h_{\min} = 1$ mm and the smoothing factor was $\beta = 3$. Figure 9 plots the density contours corresponding to the adapted meshes of Figure 8. One can clearly see that the density contours do not have any pre- and post-shock noise due to the alignment of anisotropic elements with shock waves, and the simultaneous development between anisotropic elements and the density contours. Figures 10 and 11 give two close-up views to further demonstrate the captured solution by aligned anisotropic elements. In Figure 10, the complex shock–shock interactions happening above the perforated holes are captured by anisotropic elements distributed in the direction and position the density contours indicate.

 

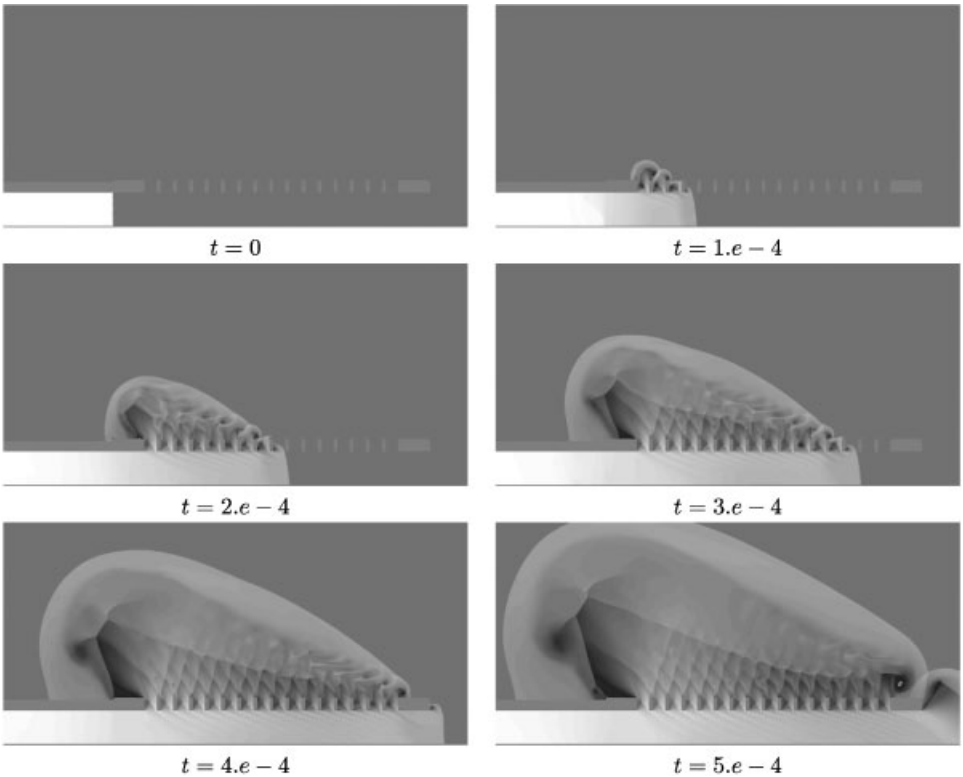


Figure 9. Evolution of the density contours in log scale for the cannon blast problem.

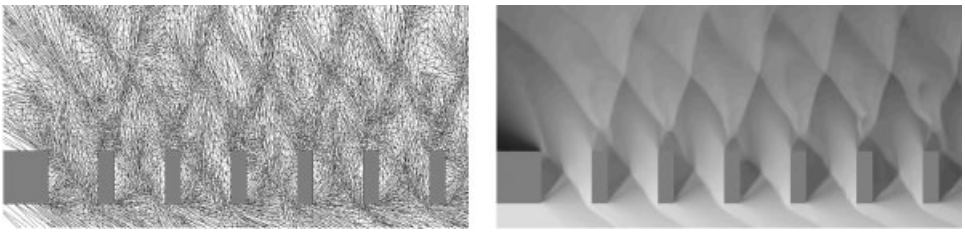

Figure 10. Complex shock–shock interaction structure near the muzzle at $t = 5.e - 4$.

In Figure 11, the zoom near the front shock shows the alignment between the anisotropic elements and the front shock.

### *5.3. Three-dimensional backward facing step*

This example simulates the shock development when a backward facing step is impulsively inserted into a Mach 3 gas flow in a straight pipe. Figure 12 shows the analysis domain. Since axisymmetric, only a small section (15°) of a cylinder is used. The cylinder is of length 7.62

 

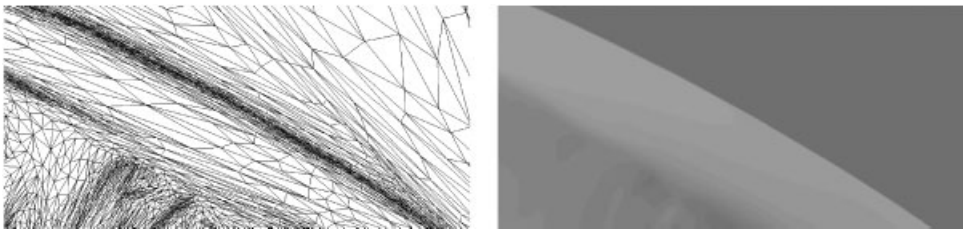

Figure 11. Zoom near to the front shock at $t = 5.e - 4$.

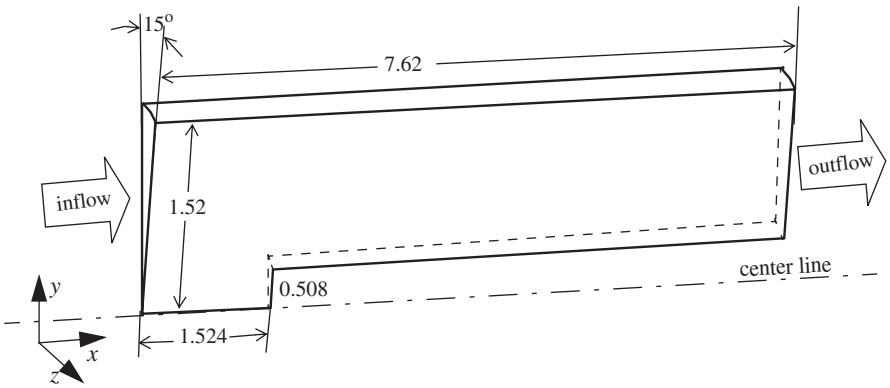


Figure 12. Simulation domain of backward step.

and of radius 1.52, and the step is situated at $x = 1.524$ and of height 0.508. The initial condition is a constant Mach 3 flow field in the $x$-axis, in particular,

$$p = 1$$

$$\rho = 1$$

$$u_1 = M_s\sqrt{\gamma} = 3\sqrt{1.4} = 3.55$$

where $p$ denotes pressure, $\rho$ denotes density, $u_1$ is the velocity in $x$ direction, $M_s$ is Mach number and $\gamma$ is gas parameter. The boundary conditions are as follows:

- At inlet and outlet, the velocity, density and pressure are that of the initial Mach 3 flow;
- At the two cut planes parallel to the centre line of the cylinder, symmetry boundary condition is applied;
- For all other surfaces, slip wall boundary condition is applied.

Starting from a uniform isotropic initial mesh of size 0.5, a steady flow pattern with shock is reached in about 4 s. The mesh is updated every $5 \times 10^{-3}$ s, therefore, a total of 800 mesh adaptations are performed. The total number of degrees of freedom in the initial mesh is 14 960 which corresponds to 748 tetrahedra. After 800 mesh adaptations, the number of degrees of

 

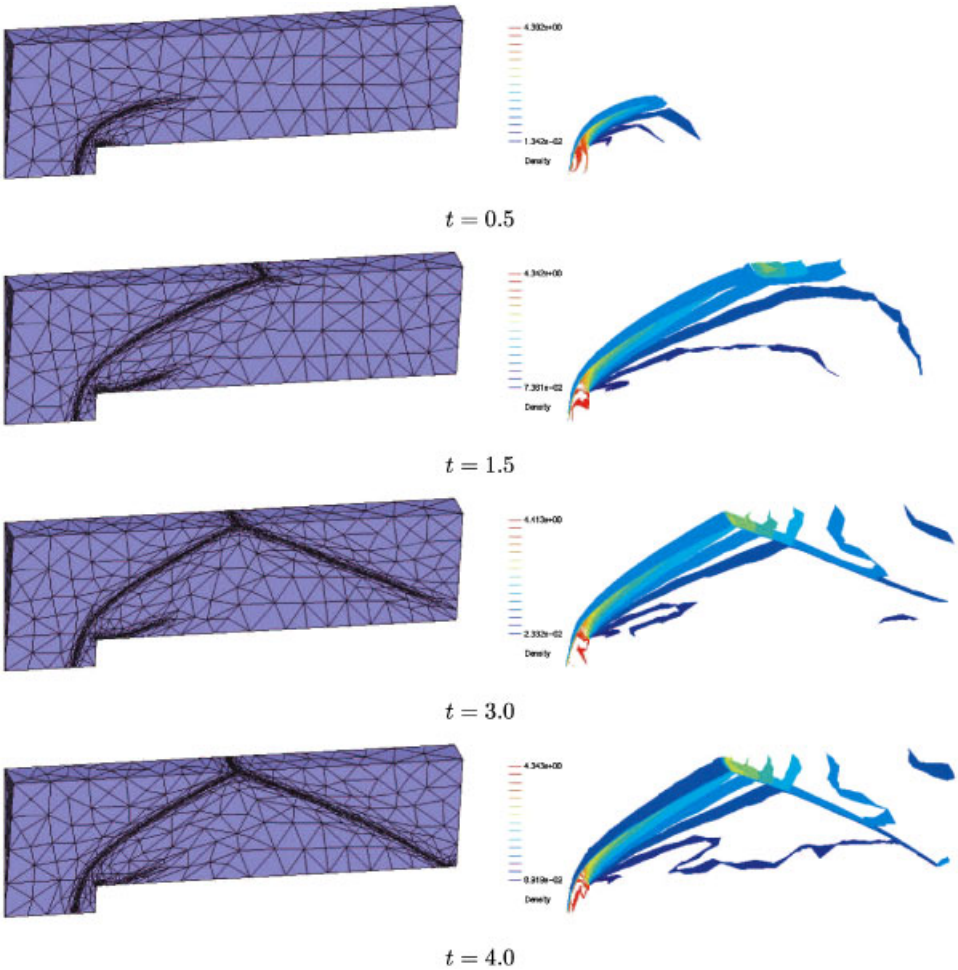


Figure 13. Evolution of mesh and density contour for backward facing step problem.

freedom reaches 96 020 which corresponds to 5081 tetrahedra. Figure 13 shows the evolution of the mesh and the corresponding density contour surface for the backward step problem. It can be seen that the mesh aligns to the discontinuity of density with anisotropic tetrahedra and develops as the discontinuity develops. Figure 14 shows a close-up view of the mesh and density contour near the top surface where the shock reflects. It can be seen that elements become needle-like where the shock strikes the top surface.

## 6. CLOSING REMARKS

A general procedure for the adaptive construction of anisotropic meshes over general two- and three-dimensional domains has been presented. Its application has been demonstrated on the

 

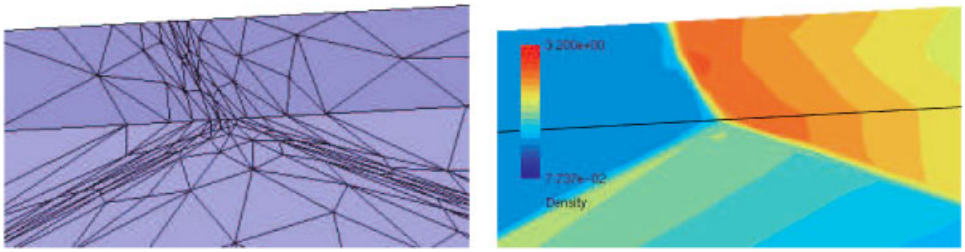


Figure 14. Zoom near the shock reflection at $t = 4$ s.

transient flow simulations that have complex evolving features. Key features of the procedures presented include:

- a general approach to the construction of an anisotropic mesh metric field capable of continued improvement as new error estimation and correction indication procedures are developed,
- a variationally based procedure to calculate higher derivatives applicable for use with discontinuous Galerkin methods,
- a procedure to detect solution discontinuities and isolate them for the generation of an appropriate anisotropic mesh at those locations,
- a set of intelligent mesh modification procedures that can modify a given mesh to match any given mesh metric field.

## ACKNOWLEDGEMENTS

The various components of this work were supported by Simmetrix Inc., the ASCI Flash Center at the University of Chicago under contract B341495, and the DOE SciDAC program through agreement DE-FC02-01-ER25460.

## REFERENCES

1. Cockburn B, Karniadakis GE, Shu C-W (eds). *Discontinuous Galerkin Methods*, vol. 11. Lecture Notes in Computational Science and Engineering. Springer: Berlin, 2000.
2. Remacle J-F, Flaherty JE, Shephard MS. An adaptive discontinuous Galerkin technique with an orthogonal basis applied to compressible flow problems. *SIAM Review* 2003; **45**(1):53–72.
3. Almeida RC, Feijoo PA, Galeao AC, Padra C, Silva RS. Adaptive finite element computational fluid dynamics using an anisotropic error estimator. *Computer Methods in Applied Mechanics and Engineering* 2000; **182**(3–4):379–400.
4. Borouchaki H, George PL, Hecht F, Laug P, Saltel. Delaunay mesh generation governed by metric specifications—Part i: algorithms and Part ii: applications. *Finite Elements in Analysis and Design* 1997; **25**:61–83, 85–109.
5. Castro-Diaz MJ, Hecht F, Mohammadi B. Anisotropic unstructured grid adaptation for flow simulations. *International Journal for Numerical Methods in Fluids* 1997; **25**(4):475–491.
6. George PL, Hecht F. Non isotropic grids. In *CRC Handbook of Grid Generation*, Thompson J, Soni BK, Weatherill NP (eds). CRC Press: Boca Raton, 1999; 20.1–20.29.
7. Goodman J, Samuelsson K, Szepessy A. Anisotropic refinement algorithms for finite elements. *Technical Report*, NADA KTH, Stockholm, March 1996.

 

8. Kunert G. Toward anisotropic mesh construction and error estimation in the finite element method. *Numerical Methods in Partial Differential Equations* 2002; **18**:625–648.
9. Muller J-D. Anisotropic adaptation and multigrid for hybrid grids. *International Journal for Numerical Methods in Fluids* 2002; **40**:445–455.
10. Pain CC, Umpleby AP, de Oliveria CRE, Goddard AJH. Tetrahedral mesh optimization and adaptivity for steady-state and transient finite element calculations. *Computer Methods in Applied Mechanics and Engineering* 2001; **190**:3771–3796.
11. Rachowicz W. An anisotropic *h*-adaptive finite element method for compressible Navier–Stokes equations. *Computer Methods in Applied Mechanics and Engineering* 1997; **147**:231–252.
12. Saramito P, Roquet N. An adaptive finite element method for viscoplastic fluid flow in pipes. *International Journal for Numerical Methods in Engineering* 2001; **190**:5391–5412.
13. Walkley M, Jimack PK, Berzins M. Anisotropic adaptivity for finite element solutions for three-dimensional convection-dominated problems. *International Journal for Numerical Methods in Fluids* 2002; **40**:551–559.
14. Walsh PC, Zingg DW. Solution adaptation of unstructured grids for two-dimensional aerodynamic computations. *AIAA Journal* 2001; **39**(5):831–837.
15. Ainsworth M, Oden JT. *A Posteriori Error Estimation in Finite Element Analysis*. Wiley-Interscience: New York, 2000.
16. Babuska I, Strouboulis T. *The Finite Element Method and its Reliability*. Oxford University Press: Oxford, 2001.
17. Bottasso CL, Shephard MS. A parallel adaptive finite element flow solver for rotary wing aerodynamics. *AIAA Journal* 1997; **35**(6):1–8.
18. Dindar M, Shephard MS, Flaherty JE, Jansen K. Adaptive cfd analysis for rotorcraft aerodynamics. *Computer Methods in Applied Mechanics and Engineering* 2000; **189**:1055–1076.
19. Löhner R. Some useful data structures for the generation of unstructured grids. *Communications in Applied and Numerical Methods* 1988; **4**:123–135.
20. Pirzadeh SZ. An adaptive unstructured grid method by grid subdivision, local remeshing and grid movement. *14th AIAA Computational Fluid Dynamics Conference*, *AIAA Paper 99-3255*, July 1999.
21. Van Leer B. Flux vector splitting for the Euler equations. *Technical Report*, *ICASE Report*, NASA Langley Research Center, 1995.
22. Woodward P, Colella P. The numerical simulation of two-dimensional fluid flow with strong shocks. *Journal of Computational Physics* 1984; **54**:115–173.
23. Colella P, Glaz HM. Efficient solution algorithms for the Riemann problem for real gases. *Journal of Computational Physics* 1985; **59**:264–289.
24. Biswas R, Devine KD, Flaherty JE. Parallel adaptive finite element method for conservation laws. *Applied Numerical Mathematics* 1984; **14**:255–283.
25. Remacle J-F, Pinchedez K, Flaherty JE, Shephard MS. An efficient local time stepping-discontinuous Galerkin scheme for adaptive transient computations. *Computer Methods in Applied Mechanics and Engineering* 2002, accepted.
26. Rachowicz W. An anisotropic *h*-type refinement strategy. *Computer Methods in Applied Mechanics and Engineering* 1993; **109**:169–181.
27. Zienkiewicz OC, Zhu JZ. Superconvergent patch recovery and a posteriori error estimates. Part 1: the recovery technique. *International Journal for Numerical Methods in Engineering* 1992; **33**(7):1331–1364.
28. LeVeque R. *Numerical Methods for Conservation Laws*. Birkhäuser-Verlag: Basel, 1992.
29. van Leer B. Towards the ultimate conservation difference scheme, II. *Journal of Computational Physics* 1974; **14**:361–367.
30. van Leer B. Towards the ultimate conservation difference scheme, V. *Journal of Computational Physics* 1979; **32**:1–136.
31. Cockburn B, Shu C-W. TVB Runge–Kutta local projection discontinuous Galerkin methods for scalar conservation laws II: general framework. *Mathematics of Computation* 1989; **52**:411–435.
32. Biswas R, Devine K, Flaherty JE. Parallel adaptive finite element methods for conservation laws. *Applied Numerical Mathematics* 1994; **14**:255–284.
33. Adjerid S, Devine KD, Flaherty JE, Krivodonova L. A posteriori error estimation for discontinuous Galerkin solutions of hyperbolic problems. *Computer Methods in Applied Mechanics and Engineering* 2002; **191**: 1097–1112.
34. Li X, Remacle J-F, Chevaugeon N, Shephard MS. Anisotropic mesh gradation control. *13th International Meshing Roundtable*, 2004.

 

35. Li X. Mesh modification procedures for general 3-D non-manifold domains. *Ph.D. Thesis*, Rensselear Polytechnic Institute, August, 2003.
36. Li X, Shephard MS, Beall MW. 3-d anisotropic mesh adaptation by mesh modifications. *Computer Methods in Applied Mechanics and Engineering*, 2003, submitted.
37. Thomas Tracy Y. *Concepts from Tensor Analysis and Differential Geometry*. Academic Press: New York, 1965.
38. Liu A, Joe B. On the shape of tetrahedra from bisection. *Mathematics of Computations* 1994; **63**:141–154.
39. Mavriplis DJ. Adaptive mesh generation for viscous flows using delaunay triangulation. *Journal of Computational Physics* 1990; **90**:271–291.
40. Bornemann F, Erdmann B, Kornhuber R. Adaptive multilevel methods in three space dimensions. *International Journal for Numerical Methods in Engineering* 1993; **36**:3187–3203.
41. de Cougny HL, Shephard MS. Parallel refinement and coarsening of tetrahedral meshes. *International Journal for Numerical Methods in Engineering* 1999; **46**:1101–1125.
42. Liu A, Joe B. Quality local refinements of tetrahedral meshed based on bisection. *SIAM Journal on Scientific Computing* 1995; **16**:1269–1291.
43. Briere de I'Isle E, George PL. Optimization of tetrahedral meshes. In *Modeling*, *Mesh Generation*, *and Adaptive Numerical Methods for Partial Differential Equations*, Babuska I, Flaherty JE, Henshaw WD, Hopcroft JE, Oliger JE, Tezduyar T (eds). Springer: Berlin, 1993; 97–128.
44. Tam CKW, Webb JC. Dispersion relation preserving finite difference schemes for computational acoustics. *Journal of Computational Physics* 1993; **107**:262–281.

 